

Chapter 4

Dilute Fe doped $Sb_{1-x}Se_x$ and SbSe bi-layer thin film system

The purpose of the present chapter is, to study the dilute Iron doped Antimony rich SbSe thin films grown on Silicon substrate using physical vapor deposition technique and Sb-Se bi-layer thin films grown on quartz substrates. This chapter is divided into two sections.

In the first section, dilute Fe doped $Sb_{1-x}Se_x$ thin films having composition $Fe_{0.008}Sb_{1-x}Se_x$: with Selenium concentration variation ($x = 0.01, 0.05$ and 0.10) is discussed using various characterizations as: structural, electrical, charge carrier concentration properties, optical, surface morphological and magnetic properties.

In the second section, Annealing and irradiation effects in Sb-Se bi-layer thin films: The effects of Se layer's thickness variations in Sb-Se Bilayer thin films grown on quartz substrate using thermal evaporation technique are discussed. Comparative study of pristine Sb-Se and annealed bilayer thin films of various thicknesses is discussed. This includes structural, electrical, surface morphological and compositional studies.

4.1 Dilute Fe doped $\text{Sb}_{1-x}\text{Se}_x$ thin films

4.1.1 Introduction

The study of magnetic semiconductors is their potential of combining semiconducting and magnetic behavior in a single material system. Such a combination facilitates the integration of magnetic components, into existing semiconducting processing methods. Thus provides compatible semiconductor–ferromagnet interfaces. As a result, DMSs are viewed as enabling materials for the emerging field of magneto-electronic devices and technology. Because such devices exploit both the facet of the electron's spin as well as charge. They are known as spintronic devices. In addition to their potential technological interest, the study of magnetic semiconductors is revealing a wealth of new and fascinating physical phenomena, including persistent spin coherence, novel ferromagnetism, and spin-polarized Photoluminescence [1].

DMSs are materials based on II-VI, III-V and IV-IV compound semiconductors have been of interest as they combine the two large branches in condensed matter physics; semiconductor and magnetism. These kinds of materials are also very attractive for technological point of view since there is exploitation of the spin of the electron, in addition to its charge, to create a new class of spin transport electronic devices [2-3]. DMS is a functional material which is magnetized by introducing local magnetic moments into the host by substitution of transition metals like Mn, Fe, Co, Ni or rare earth metals. Different preparation techniques have been adopted to raise the Curie temperature to RT in various DMS materials [4-6]. Charge carrier induced ferromagnetic interaction is proposed as a mechanism for these systems [7-8]. A lot of work has been done with doping of different transition metals in CdTe [9], CdSe [10-11], InSb [12] and ZnO [13]. Some of the studies like S. A. Gad *et.al.* [9] reported the structural and optical properties of $\text{Cd}_{1-x}\text{Mn}_x\text{Te}$ DMS system, J. A. Peters *et. al.* [12]

reported the Magneto-transport properties of $\text{In}_{1-x}\text{Mn}_x\text{Sb}$ magnetic semiconductor thin films whereas S. Riaz *et. al.* [14] reported RT ferromagnetism in Sol-gel deposited un-doped ZnO films.

Zayed *et. al.* [15] reported the structural and electrical properties of un-doped $\text{Sb}_{1-x}\text{Se}_x$ ($0 \leq x \leq 0.9$) thin films grown on glass and quartz substrate. He reported that the DC electrical conductivity is of the order of $10^{-12} \text{ } \Omega^{-1} \text{ cm}^{-1}$ to $10^{-2} \text{ } \Omega^{-1} \text{ cm}^{-1}$ for Selenium rich compositions and from $10^{-5} \text{ } \Omega^{-1} \text{ cm}^{-1}$ to $10 \text{ } \Omega^{-1} \text{ cm}^{-1}$ for the antimony rich compositions. They showed that for values of $x = 0, 0.1, 0.3, 0.4$ and 0.9 p-type conduction takes place, whereas for $x = 0.5$ it is n-type conduction. Kang. *et. al.* [16] reported the structural transformation of $\text{Sb}_x\text{Se}_{1-x}$ thin films for phase change nonvolatile memory application. Among many groups of semiconductors, the V-VI group semiconductor alloys doped with magnetic impurity show potential ability to form electron mediated ferromagnetism as reported in one of the earliest studies on Fe: $\text{Sb}_{1-x}\text{Se}_x$ bulk alloy [17]. The electron mediated ferromagnetism is attributed to p-d exchange & carrier induced polarization. Recently similar type of interaction in Ge based alloy thin films [18] is also reported. Although the bulk studies of Fe: $\text{Sb}_{1-x}\text{Se}_x$ showed RT magnetism [17], the properties of thin films may differ dramatically. Also the thin films are important for the application purpose. It is thought that it would be extremely useful to see characteristics of thin films. To see the properties of thin films dilute Fe (0.008) doped $\text{Sb}_{1-x}\text{Se}_x$ alloy films are prepared. Although in the literature, some work on FeSb_2 compound and alloy thin films of Fe-Sb does exist, but the concentration of Fe in Sb system is extremely high [19-21]. In a reported study on bulk $\text{Fe}_x\text{Sb}_{100-x}$, even at extremely high concentrations of Fe ($x = 0.63$), no magnetic interaction is seen [22]. No report on Fe-Sb-Se alloy thin films with Fe in such low concentration is found in literature.

In this section of the chapter, studies of very dilute Fe (0.008) doped $\text{Sb}_{1-x}\text{Se}_x$ ($x = 0.01, 0.05$ and 0.10) thin films prepared on Silicon (Si) substrate by thermal evaporation technique are discussed. Effect of Selenium concentration variation in structural, electrical, optical, surface morphology and magnetic properties of $\text{Fe}_{0.008}\text{Sb}_{1-x}\text{Se}_x$ thin films is discussed.

4.1.2 Experimental details

To prepare the thin films of $\text{Fe}_{0.008}\text{Sb}_{1-x}\text{Se}_x$ ($x = 0.01, 0.05, 0.10$) alloys, bulk alloys are prepared by arc melting of highly pure elements, namely Antimony (99.999 % Alfa Aesar), Selenium (99.999 %, Alfa Aesar) and Iron (99.998 %, Alfa Aesar) under argon atmosphere in an arc furnace. During the sample preparation oxygen contamination is avoided by evaporating the Titanium inside the vacuum chamber before the arc melting. To get the homogeneity in the sample, the melting process is repeated many times. During the melting process weight-loss of the sample is less than 0.5 %.

After the preparation process of bulk alloys, the Fe doped $\text{Sb}_{1-x}\text{Se}_x$ thin films are deposited on Si substrate by thermal evaporation technique with varying Selenium concentration for $x = 0.01, 0.05$ and 0.10 respectively. The Silicon substrate is put on the top of a Molybdenum crucible boat loaded with $\text{Fe}_{0.008}\text{Sb}_{1-x}\text{Se}_x$ (for $x = 0.01, 0.05$ and 0.10 respectively) and evaporated using resistive heating in $> 10^{-5}$ Torr. To get rid of the contamination, the substrate is cleaned properly prior to deposition. Deposited thin films are annealed at $300\text{ }^\circ\text{C}$ temperature at 5×10^{-5} Torr for 1 hour to release stress. It also enhances better adhesion between the films and substrate. The measured thickness of the films is ~ 500 nm using Fizeau fringes.

The structural study of alloy thin films is done by Grazing Angle X-ray Diffraction (GAXRD) technique using Bruker D8 Advance X-ray diffractometer. The

X- rays are produced using a sealed tube and the wavelength of X- rays are 0.154 nm (Cu K- alpha). The X- rays are detected using a fast counting detector based on silicon strip technology (Bruker LynxEye detector). This configuration allows the use of a Grazing Angle X-ray Diffraction (GAXRD). This XRD pattern is monitored at RT with a constant rate of 0.05 degree/3s at grazing angle (α) 0.5°. The optical study of the thin films is done using PL measurement at RT using Spectrofluorophotometer. The resistivity measurement is done on these thin films using four probe method in the temperature range of 100-350 K. For this study Indium is used to make contact. The whole resistivity set-up unit is kept in a cryostat and the resistance is measured by Keithley 617 programmable electrometer connected to the DC Power supply [23]. The sample surface is analyzed using Atomic Force Microscope (AFM) from Digital Instruments (Nanoscope III) with Si₃N₄ tips under ambient conditions in the contact mode at RT. This provides high resolution surface micrographs. Magnetic imaging of sample surface as a function of the Se concentration is carried out by a magnetic force microscope (MFM) from the Nano magnetic instrument at RT. AFM and MFM are employed to spatially probe the structure of the sample surfaces and distribution of the local magnetic field.

4.1.3 Structural studies

The X- ray diffraction pattern of as deposited dilute Fe (0.008) doped Sb_{1-x}Se_x (x = 0.01, 0.05, 0.10) alloy thin films is shown in **figure 4.1**.

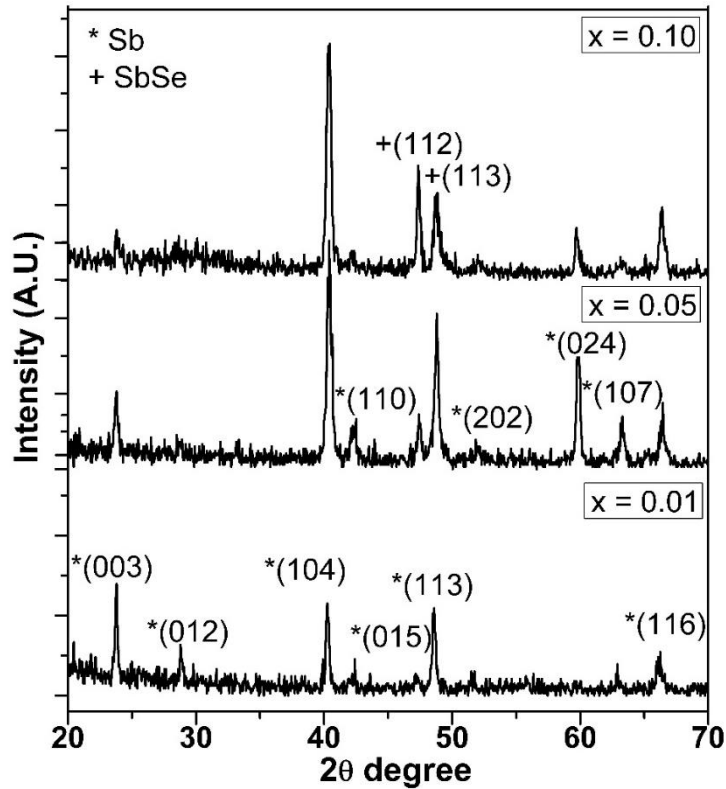


Figure 4.1: XRD spectra of $Fe_{0.008}Sb_{1-x}Se_x$ ($x = 0.01, 0.05$ and 0.10) thin films grown on Si substrate

In this diffraction pattern the observed peak positions at 23.8° (003), 28.8° (012), 40.3° (104), 42.4° (110), 47.1° (015), 48.5° (113), 51.5° (202), 60° (024), 63.1° (107), 66.4° (116) matches with the JCPDS card of the Sb (ASTM-JCPDS card no. 85-1324). This indicates the formation of polycrystalline rhombohedral Sb structure. In this diffraction pattern it is observed that there are two merged peaks at two different peak positions viz. 47.2° (112) and 48.3° (200) these peaks seems to be of Sb-Se compound phase. The intensity of these Sb-Se peaks increases with increase in Se concentration. However, no peaks of Fe or Fe related magnetic phases with Sb or Se is observed in the XRD pattern. With the increase in Se concentration there are relative changes in the intensity and small shifts in XRD peak position indicating that Se is getting incorporated into the alloy thin films.

The crystallite size is calculated by using the Debye Scherrer Formula *i.e.*

$$D = \frac{0.89\lambda}{\beta \cos\theta}$$

Where D is crystallite size, λ is the wavelength of X-rays, θ is the angle of diffraction, and β is the broadening of the diffraction line measured at half its maximum intensity in radians. The average crystallite size of the Fe doped $\text{Sb}_{1-x}\text{Se}_x$ thin films is found to be in between ~ 14-19 nm for $x = 0.01- 0.10$ shown in **table 4.1**. With the increase in Se concentration peaks becomes more intense and sharper *i.e.* crystallinity of thin film increases with Se concentration.

Sample composition	Structural parameters
$\text{Fe}_{0.008}\text{Sb}_{1-x}\text{Se}_x$	Crystallite Size (nm)
$x = 0.01$	14.2
$x = 0.05$	15.9
$x = 0.10$	18.8

Table 4.1: Structural parameters of $\text{Fe}_{0.008}\text{Sb}_{1-x}\text{Se}_x$ for $x = 0.01, 0.05$ and 0.10 thin film system

4.1.4 Electrical Studies

The resistivity as a function of temperature is calculated from the resistance taking the geometry and film thickness of the film into account. The plotted curves for electrical resistivity ($\ln\rho$) versus $10^3/T$ with different Se concentrations ($x = 0.01, 0.05$ and 0.10) are shown in **figure 4.2**. All the films (for $x = 0.01, 0.05$ and 0.10) show very low resistivity (order of 10^{-3}) and varies from 0.05 to $0.10 \times 10^{-3} \Omega\text{-cm}$. Below RT resistivity increases linearly with temperature, which clearly show the metallic nature of the alloys having positive Temperature Coefficient of Resistance (TCR). However, resistivity starts decreasing above RT indicating a phase transition, *i.e.* metal to semiconductor phase transition taking place [24]. This transition from positive TCR to negative TCR seems to be due to the formation of some compound phase of Sb-Se [24].

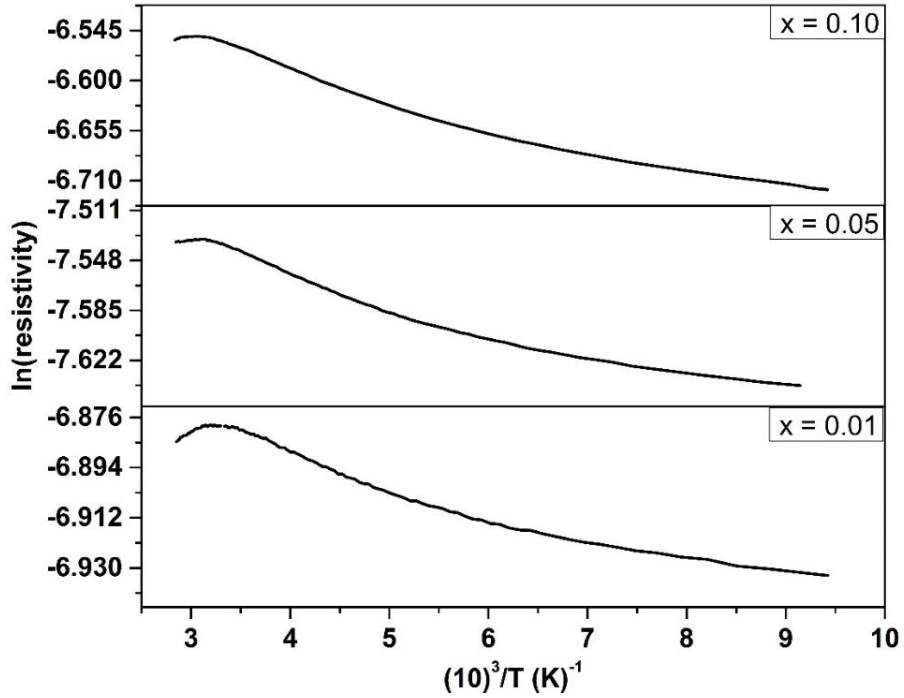


Figure 4.2: $(10)^3/T$ vs. $\ln(\text{resistivity})$ spectra of $\text{Fe}_{0.008}\text{Sb}_{1-x}\text{Se}_x$ thin films for different Se concentration: $x = 0.01, 0.05, 0.10$.

This compound phase formation decreases the charge carrier density as discussed later in our Hall Effect study. With the increase in Se concentration (from $x = 0.01$ to 0.10) there is an observed shift of transition regime from 305 to 328 K *i.e.* towards higher temperature which supports the probability of compound phase formation of Sb-Se. This shift in temperature increased from 305 to 328 K is shown in **table 4.2**. It indicates that the transition temperature can be tuned with Se concentration which is supported by the argument of diffusion probability.

Sample composition	parameters calculated from resistivity measurement		
	Activation energy (meV)	Transition Temperature (K)	Temperature coefficient of resistance ($^{\circ}\text{C}^{-1}$)
$x = 0.01$	1.09	305	2.96×10^{-4}
$x = 0.05$	2.09	320	5.78×10^{-4}
$x = 0.10$	3.21	328	8.64×10^{-4}

Table 4.2: Electrical parameters of $\text{Fe}_{0.008}\text{Sb}_{1-x}\text{Se}_x$ for $x = 0.01, 0.05$ and 0.10 thin film system

The value of TCR increases from $2.96 \times 10^{-4} \text{ }^\circ\text{C}^{-1}$ to $8.64 \times 10^{-4} \text{ }^\circ\text{C}^{-1}$ with the increase in values of Se concentration in the temperature range 100 to 250 K. The value of TCR is shown in **table 4.2**. These results are used to calculate activation energy below the transition region using Arrhenius Equation [25].

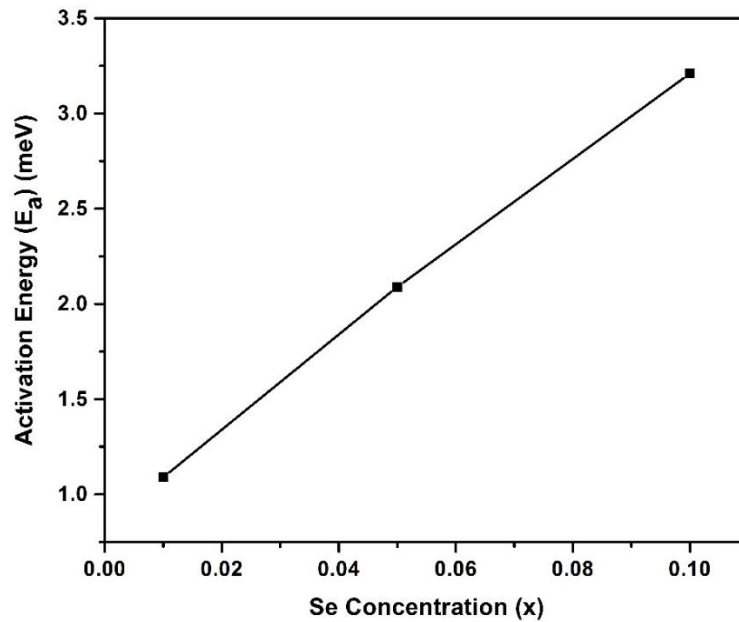


Figure 4.3: Se concentration (x) vs. Activation Energy (E_a) plot of $\text{Fe}_{0.008}\text{Sb}_{1-x}\text{Se}_x$ thin films
i.e.

$$R(t) = R_0 \exp(E_a/K_b T)$$

Where $R(t)$ is resistivity at temperature T , E_a is the Activation energy and K_b is the Boltzmann constant. The activation energy is plotted as a function of the Se concentration (x) is shown in **figure 4.3**. The calculated E_a for different Se concentration ($x = 0.01, 0.05$ and 0.10) is also listed in **table 4.2**. It is observed from the value of the activation energy for different x that with the increase in Se concentration, the activation energy increases linearly from 1.09 to 3.21 meV.

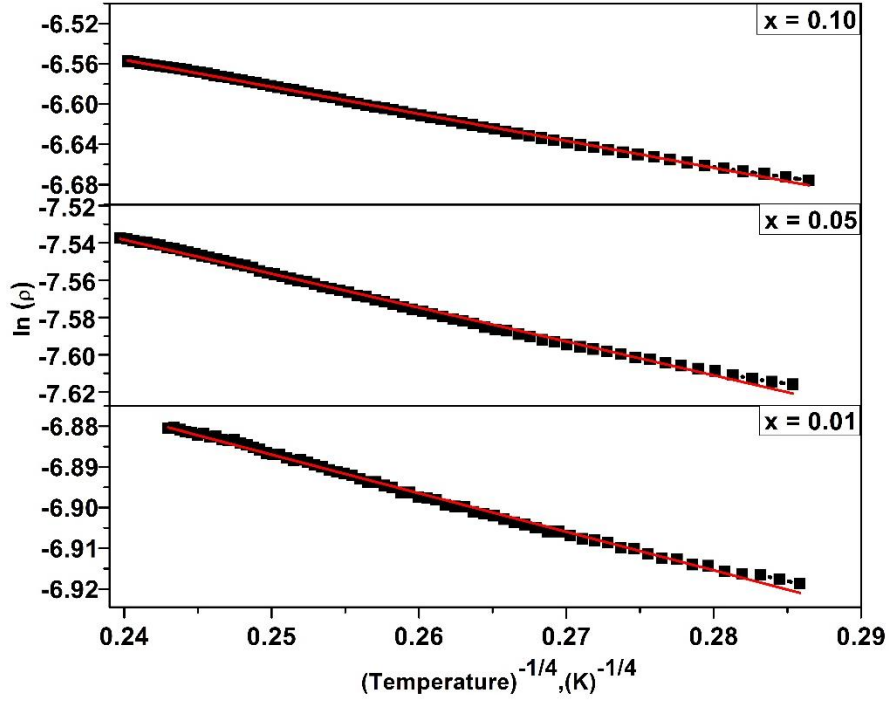


Figure 4.4: Temperature dependence of Resistivity $\rho(T)$ measured with varying concentration of Se in $Fe_{0.008}Sb_{1-x}Se_x$ thin films, by the relation based on the three-dimensional Mott's variable range hopping conduction (3D-VRH), using equation, $\rho \propto \exp(T_0/T)^{1/4}$. The solid lines are linear fit of data.

In order to explain the low temperature transport mechanism in Fe (0.008) doped $Sb_{1-x}Se_x$ thin films, the hopping conductivity in the disordered systems can be understood by Variable Range Hopping (VRH) mechanism as suggested by Ambegaokar *et. al.* [26], which fits very well in the temperature range 150-300 K. His idea is based on a model in which charge is transported by thermally assisted hopping of electrons between localized states, which are randomly distributed at energy and position. The VRH mechanism is governed by [27].

$$\rho(T) = \rho_0 \exp(T_0/T)^{1/4}$$

Where, ρ_0 and T_0 denote material parameters. Here $K_B T_0 = [1.5/\alpha^3 N(E)]$, where $N(E)$ is the density of the state at Fermi level and α denotes the rate of fall-off of the envelop of the electron wave function. The plotted normalized resistivity ($\ln \rho$) as a

function of $(1/T)^{1/4}$ is shown in **figure 4.4**. This plot is a straight line. These data (square black box) are linearly fitted (red line). The **figure 4.4** depicts both experimental and fitted values. It is observed that value of T_0 increases with the increase in Se concentration. This suggests that the density of states at the Fermi level decreases with increase in Se concentration in a $Fe_{0.008}Sb_{1-x}Se_x$ system. This result evinces the hopping of charge carriers between randomly distributed localized electronic states in the samples.

4.1.5 Photoluminescence (PL) studies

The PL emission spectra of Fe (0.008) doped $Sb_{1-x}Se_x$ thin films with varying Se concentration ($x = 0.01-0.10$) in the wavelength range 350-650 nm is shown in **figure 4.5**. These PL spectra are recorded at RT. From these spectra emission peak at 370, 384, 394 nm and shoulder at 406 nm are observed. In addition to this there are two broad peaks at 452 and 471 nm. It is also seen that with the increase in Se concentration in the system number of impurity peaks increased (maximum no. of impurity peaks at $x = 0.10$).

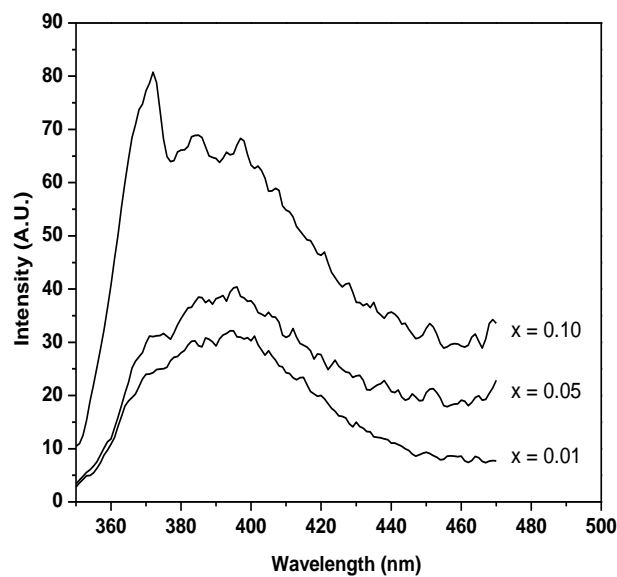


Figure 4.5: PL spectra of $Fe_{0.008}Sb_{1-x}Se_x$ at $x = 0.01, 0.05$ and 0.10

This observation suggests that there is an increase in the crystallinity of the material, with an increase in the Se concentration. This is also supported by the observed XRD patterns. Due to increase in crystallinity of the host material, the energy levels become more discrete resulting into more intense electronic transitions corroborated by an increase in the energy at 365 nm and intensity of the PL peak.

4.1.6 Hall Measurement

The Hall Measurement is performed on these thin films at RT for different Se concentrations for $x = 0.01, 0.05$ and 0.10 . It is observed from the Hall studies that charge carrier concentration decreases from 2.02×10^{20} to $1.47 \times 10^{20} \text{ cm}^{-3}$ with the increase in Se concentration from 0.01 to 0.05 . In the $\text{Fe}_{0.008}\text{Sb}_{1-x}\text{Se}_x$ thin films, Selenium acts as a donor in Antimony and with increase in the Se concentration the charge carrier concentration should also increase. But surprisingly the carrier concentration decreases with increase in Se concentration from $x = 0.01$ to 0.05 . It may be due to the formation of Sb-Se compound phase in the thin film resulting in decrease in charge carrier. With further increase in the value of Selenium to $x = 0.10$, the charge carrier almost remains same $\sim 1.49 \times 10^{20} \text{ cm}^{-3}$. For low temperature Hall measurement performed at 77 K for $x = 0.10$. At temperature 77 K for $x = 0.10$ the charge carrier concentration is found to be $\sim 1.10 \times 10^{17} \text{ cm}^{-3}$.

4.1.7 Surface morphological studies

The surface morphological studies of the Fe doped $\text{Sb}_{1-x}\text{Se}_x$ thin films for different Se concentration is studied by using atomic force microscope (AFM) over $1 \times 1 \mu\text{m}^2$ area. The results are displayed in two dimensional and three dimensional images of **figure 4.6**. These AFM images are analyzed in terms of surface particle size and root mean square (rms) roughness. From the figure one can observe that smooth and adherent films are obtained.

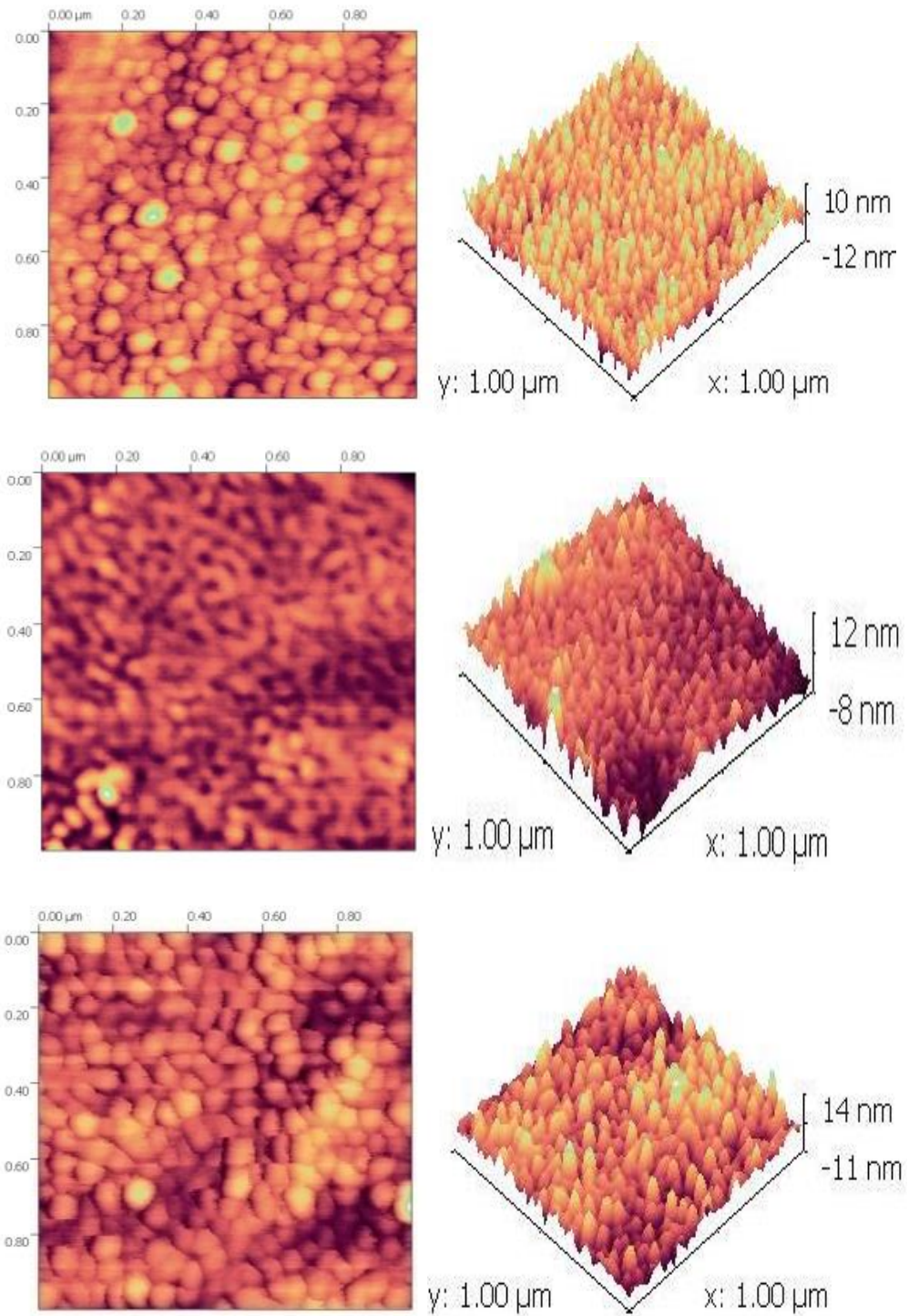


Figure 4.6: Surface morphological (AFM) two dimensional (left side) and 3-Dimensional (right side) images of $Fe_{0.008}Sb_{1-x}Se_x$ for $x = 0.01, 0.05$ and 0.10 respectively

The values of average particle size and rms roughness as obtained from these studies are given in **table 4.3**. These AFM images show almost uniform particle size distribution.

Sample composition	AFM	
$Fe_{0.008}Sb_{1-x}Se_x$	Average Particle size (nm) with standard deviation	Average rms roughness over $1 \times 1 \mu m^2$ (nm)
x = 0.01	47 ± 4	1.78
x = 0.05	53 ± 5	2.93
x = 0.10	61 ± 5	3.01

Table 4.3: Surface morphological parameters of $Fe_{0.008}Sb_{1-x}Se_x$ for x = 0.01, 0.05 and 0.10 thin film system

The particle size increases from 47-61 nm with increase in Se concentration for x = 0.01- 0.10 respectively. With the increase in Se concentration surface morphology of the films is found to change continuously that might be due to degradation in amorphous quality *i.e.* crystallinity enhances. The root mean squared (rms) surface roughness also increases with the increase in Se concentration.

4.1.8 MFM studies

The **figure 4.7** shows AFM images (left side) and MFM images (right side) of the same area of $1 \times 1 \mu m^2$ for the x = 0.01, 0.05 and 0.10 in $Fe_{0.008}Sb_{1-x}Se_x$ thin films respectively. The magnetic domain size as obtained from the **figure 4.7** is given in **table 4.4**.

Sample composition	MFM
$Fe_{0.008}Sb_{1-x}Se_x$	Average magnetic domain size (nm) With standard deviation
x = 0.01	54 ± 4
x = 0.05	63 ± 4
x = 0.10	69 ± 4

Table 4.4: Magnetic (MFM) parameters of $Fe_{0.008}Sb_{1-x}Se_x$ for x = 0.01, 0.05 and 0.10 thin film system

The diameter of the domains is measured in case of circular domains, length and breadth of the domains in the case of rectangular like domains & major and minor axis

in case the domains that are like elliptical, and equated them to an equivalent circle to get the domain size [28]. On comparing the AFM and MFM images, it can be seen that several dark spots in MFM images are not similar in contrast to the AFM image. It indicates the absence of surface effects.

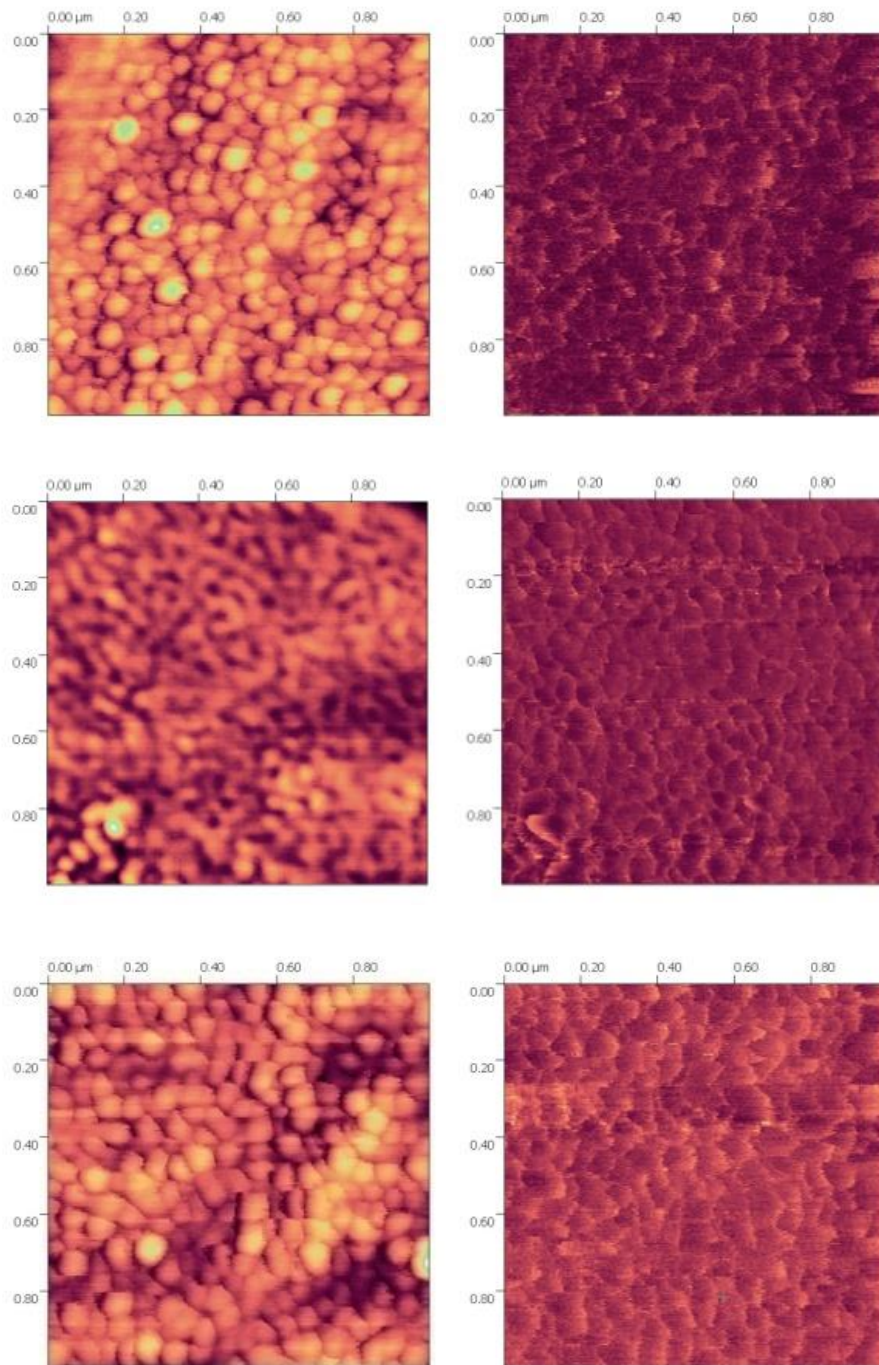


Figure 4.7: Topography AFM image (left) and corresponding MFM image (right) of the same area of $1 \times 1 \mu\text{m}^2$ for $x = 0.01, 0.05$ and 0.10 in $\text{Fe}_{0.008}\text{Sb}_{1-x}\text{Se}_x$ thin film respectively

Hence the magnetic signals observed may be due to intrinsic magnetic properties of the alloy. However the brightness in MFM images being almost uniform with small variation supports the absence of magnetic clusters, as magnetic clusters are expected to give large contrast.

Also in XRD spectra no peaks of Fe or magnetic phases of Fe with Sb or Se is observed. This also supports the absence of clusters or magnetic phases in the films. It seems that the magnetic interactions at RT is not due to any Fe clusters or magnetic phases of Fe but could be due to long range ordering of Fe local moments mediated by electron charge carriers introduced via Se doping in Fe-Sb system. This type of interaction is also observed by us in bulk studies of the same system in the concentration range of $0.01 < x < 0.02$ of Se [14].

4.2 Annealing and irradiation effects in Sb-Se bi-layer thin film

4.2.1 Introduction

The bilayer and multilayer thin films are becoming increasingly important in the development of faster, smaller and more efficient electronic and optoelectronic devices [29]. The III-V, V-VI and IV-VI semiconductors are of importance for their various applications in electro-optical device and infrared detectors [30]. Various studies on the III-V, IV-VI bilayer thin film systems [31-34] are reported. R. K. Mangal *et. al.* [31-32] studied the bilayer thin film of III-V compound as Al-Sb [31] and In-Sb [32] and compared the annealed films with as deposited films. M. Singh *et. al.* [33] characterized the Zn-Se bilayer thin film for structural, optical and thermopower properties. P M P Salome *et. al.* [34] studied the Mo bilayer thin film for photovoltaic properties and they compared the bilayer films with varying thickness for various studies. There are many other studies of bilayer films of different systems [35-38] for various application purposes.

The studies of V-VI group elements like Sb_2Te_3 , Bi_2Te_3 [39] and SbSe [40-42] are particularly important for their photovoltaic properties and high thermo-electric power, which allows possible applications for optical and thermo-electric cooling devices. P P Pradyumanan *et. al.* [39] reported the thickness variation study of Bi_2Te_3 , Sb_2Te_3 bilayer thin films which are prepared using thermal evaporation technique. They reported the effect of annealing on structural, electrical and thermo-electrical properties and concluded that bilayer films of Bi_2Te_3 - Sb_2Te_3 have more thermo-electric power at RT. K. Y. Rajpure *et. al.* [40] reported the effect of substrate temperature on the spray deposited Sb-Se bilayer thin films. K. Kolev *et. al.* [41] reported CW laser induced

transformation of Sb, Se and Sb₂Se₃ thin film in the air. This transformation of Sb, Se and Sb₂Se₃ occurs via thermal mechanism. It is observed that the transformations are drastically accelerated when the temperature attains critical value. While in another study by K. Kolev *et. al.* [42] reported synthesis of Sb₂Se₃ films using Argon laser irradiation from Sb-Se bilayer films. These films are analyzed with optical and X-ray photoelectron spectroscopies. The result gives the good reflectivity contrast between as grown and synthesized films. Due to extremely important applications of SbSe system, bilayer thin film of Sb and Se of different thickness of Se layer is prepared. The comparative studies of as deposited annealed and irradiated Sb-Se bilayer thin films are studied.

4.2.2 Experimental Techniques

To prepare Sb-Se bi-layer thin films high purity antimony (99.999%) and Selenium powder (99.999%) are used. The films are grown on quartz substrate using thermal evaporation technique. The quartz substrates are placed in substrate holders above the boat carrying materials. The antimony is first evaporated and then Selenium is deposited. The thickness of Se layer deposited is 503 Å, 301 Å & 100Å, whereas the thickness of Sb is 1015, 1013 and 1033Å (named as SbSe1, SbSe2 & SbSe3 respectively) to get Sb-Se bi-layer structure. The effect of vacuum annealing and irradiation on these thin films is studied.

A set of these thin films is annealed at 473 K temperature at a $> 10^{-5}$ Torr pressure for mixing the bilayers for two hours and another set of the sample is irradiated with 200 MeV Ag¹⁵⁺ ions using a 15 UD Tandem Accelerator, at Inter University Accelerator Centre (IUAC) New Delhi with influence of 5×10^{12} ions per cm². Irradiation process is done at RT. The ion beam is focused to a spot of 1 mm diameter and scanned over a 1.1×1.1 cm². The radiation beam is focused to cover the whole sample.

To see the structural, electrical, microstructural and surface morphological effects on annealing and irradiation on these thin films various characterization techniques like GAXRD, four probe resistivity, Scanning electron microscopy and AFM measurements is done respectively. EDXA measurement is done on un-irradiated thin films to observe the composition of the films.

The binary thin films of Sb-Se are characterized by Grazing Angle X-ray diffraction (GAXRD) technique using Cu-K α radiation source (wavelength 1.54Å) scanned between 20 to 65° 2 θ range with a grazing angle (α) at 0.5°. Resistivity measurements are carried out by the conventional Four-Probe Method. Scanning images are observed by using a model JOEL-JSM 5600 equipped with EDXA analysis [43]. The sample surface is analyzed using AFM from Nanoscope III Digital Instrument.

4.2.3 Structural studies

The **figure 4.8(a-c)** shows the X-ray diffraction pattern (GAXRD) of as deposited (**figure 4.8(a)**) Annealed (**figure 4.8(b)**) and (**figure 4.8(c)**) irradiated bi-layer Sb-Se thin films grown on quartz substrates. The thickness of Antimony is ~1000 Å and thickness of Selenium variation is 100 Å, 300 Å & 503 Å respectively. It is observed from the XRD spectra of annealed films, that there is no noticeable change due to annealing as compare to as deposited film. It is also seen that from the XRD pattern of as deposited and annealed SbSe bilayer thin films (**figure 4.8(a)** and **4.8(b)**) the reflections at 23.6° (003), 40.2° (104), 47.3° (015), 48.5° (113) and 66.4° (116) are due to the Antimony rhombohedral structure. These peaks match with the JCPDS card no. 85-1324.

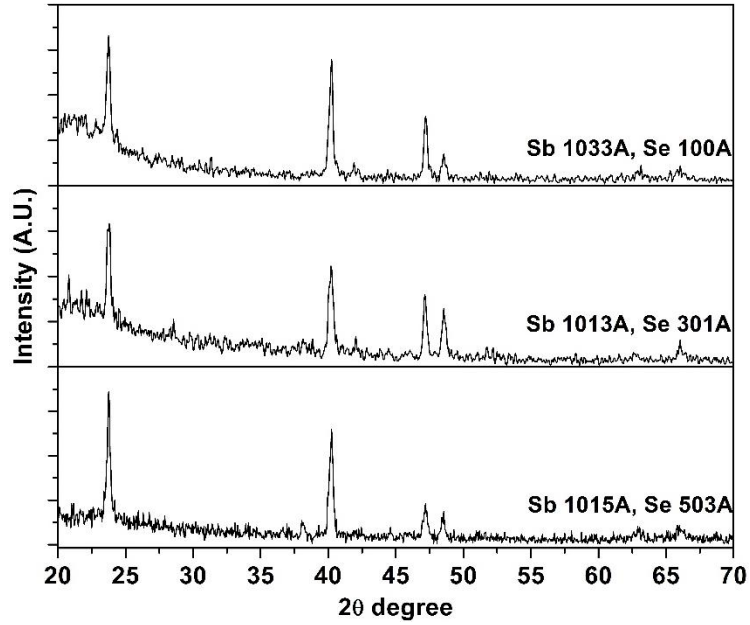


Figure 4.8(a): X-ray diffraction pattern of as deposited Sb-Se bilayer thin film

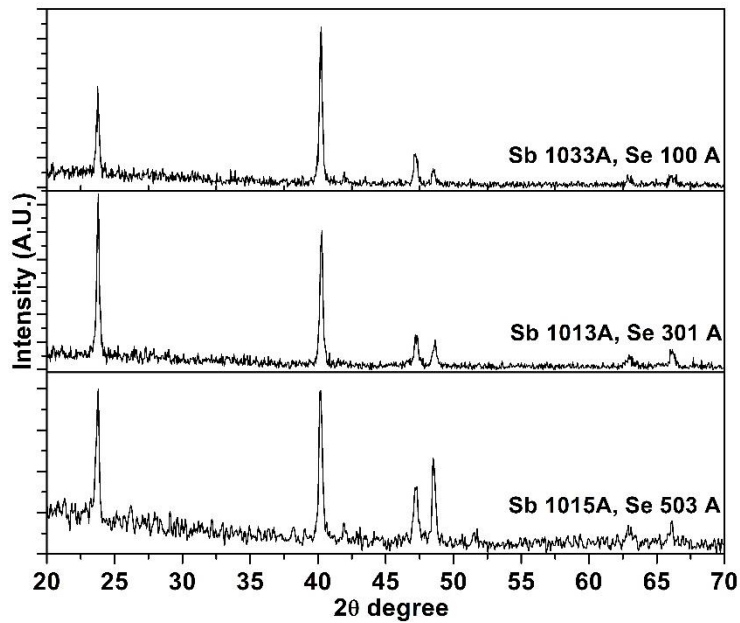


Figure 4.8(b): X-ray diffraction pattern of annealed Sb-Se bilayer thin film

The irradiation in the Sb-Se bilayer is done with the expectation that due to the irradiation process Sb and Se layer will interact and SbSe alloy or compound phase of Sb-Se will be observed. But on irradiation of as grown films with 200 MeV Ag^{+15} ions at fluence of 5×10^{12} ions per cm^2 , the peak at ~ 40 degree vanished.

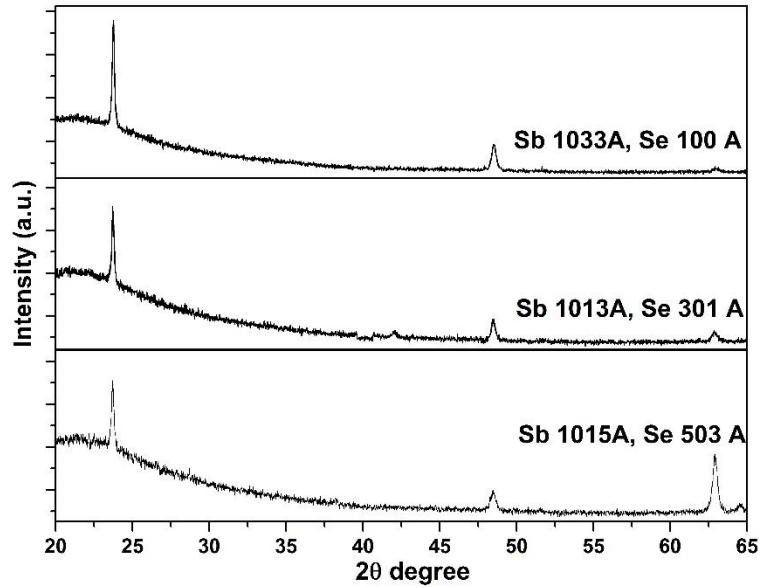


Figure 4.8(c): X-ray diffraction pattern of irradiated Sb-Se bilayer thin film

The XRD spectra of the irradiated films with SHI beam (**figure 4.8(c)**) matches with the JCPDS card of the Se cluster. Hence, with SHI instead of the formation of Sb-Se alloy it is seen that Se clusters are formed. It should be noted that the vapor pressure of Selenium is extremely high as compared to Antimony. Due to extremely high temperature exposure due to prolonged SHI irradiation, it seems that Se due to its high vapor pressure, becomes mobile and clusters of Se are observed in Sb-Se bilayer films instead of the formation of any compound phase or alloy of SbSe. After this irradiation process transition metal implantation is planned, but didn't observed SbSe alloy and hence implantation is cancelled.

The quantitative analysis of XRD data in terms of strain broadening and crystallite size is done using Williamson – Hall equation [44] given by

$$\beta \cos \theta = \frac{0.89\lambda}{D} + 4\varepsilon \sin \theta$$

This equation distinguishes strain broadening and broadening due to crystallite size. Here β is Full Width at Half Maxima (FWHM) determined from the XRD pattern, D is the crystallite size, θ is Bragg angle and λ is the wave length of X-rays used and ε

is the strain. The crystallite size for different thickness of Se, for as deposited, annealed and irradiated films are shown in **table 4.5** respectively.

Sample	crystallite size (nm)		
	as deposited	annealed	Irradiated
SbSe3	15.72	16.48	28.09
SbSe2	14.71	15.41	26.21
SbSe1	12.36	14.77	22.27

Table 4.5: Structural parameters calculated from XRD analysis for as deposited, annealed and irradiated samples respectively.

The **table 4.5** shows that the crystallite size decreases with the increase in the thickness of Selenium layer. It is also observed from the table that the crystallite size increases after annealing and irradiation of the respective films. The irradiated films have higher crystallite size as compared to the as deposited and annealed films.

4.2.4 Electrical studies

To examine the temperature dependence of the resistivity, electrical resistivity measurements are done by four probe method for the temperature range of 80-300 K for SbSe1 (thickness of Sb 1013Å & Se 503 Å).

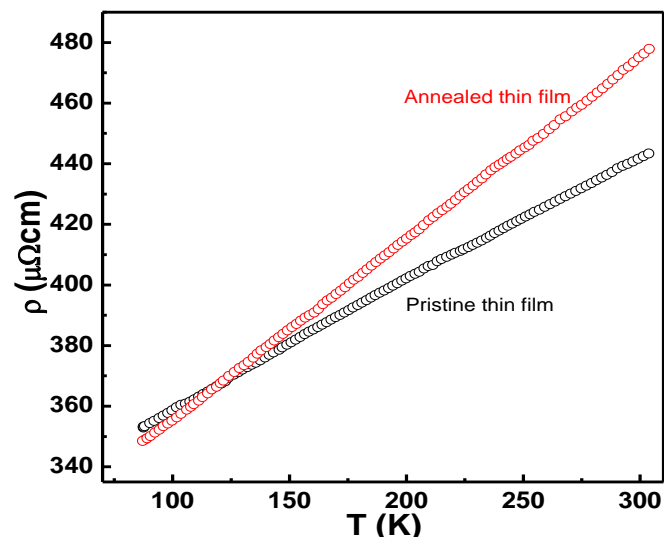


Figure 4.9: Resistivity measurement of binary Sb-Se thin film with Sb = 1015 Å and Se = 503 Å (SbSe1) thickness

The four probe method is discussed in chapter 2. The plots drawn of electrical resistivity (ρ) versus temperature (T) for as deposited and annealed SbSe1 thin films are shown in **figure 4.9**. It is observed from the **figure 4.9** that the electrical resistivity linearly increases with the increase in temperature, which indicates the metallic behavior having positive Temperature Coefficient of Resistance (TCR) of binary Sb-Se thin films. It also reveals from the **figure 4.9** that the resistivity of the annealed SbSe1 film is higher as compared to the as deposited film at higher temperature. From the Arrhenius plot (plots in between ‘ $\ln\rho$ ’ versus ‘ $1/T$ ’) the activation energy is calculated using Arrhenius Equation [45]. The calculated activation energy for SbSe1 (thickness of Sb 1015 Å & Se 503 Å) as deposited and annealed thin films are 4.31 meV & 7.13 meV observed respectively.

4.2.5 EDXA studies

To see the composition of the thin films EDXA is done on as grown films. The EDXA peaks for SbSe1 and SbSe3 are shown in **figure 4.10** and **4.11** respectively. The peaks of Sb and Se are resolved with atomic concentration of 68.30 % & 31.70 % for SbSe1 and 89.59 % & 10.41 % for SbSe3 respectively. EDXA characterization depicts the proper composition (atomic percentage) of Sb & Se according to thickness.

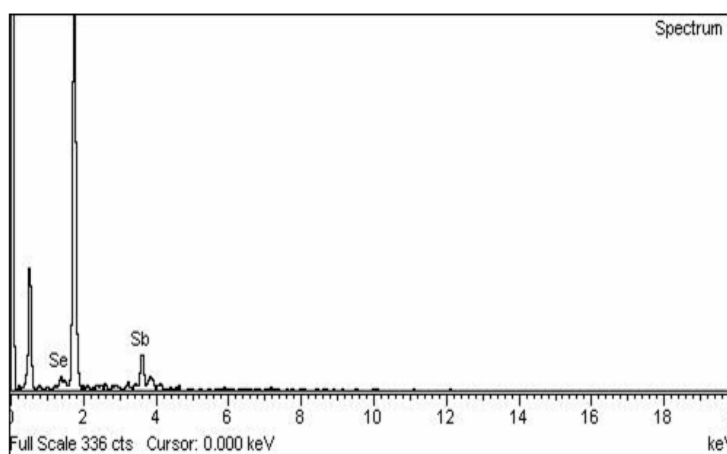


Figure 4.10: EDAX spectrum of SbSe1 as deposited thin film

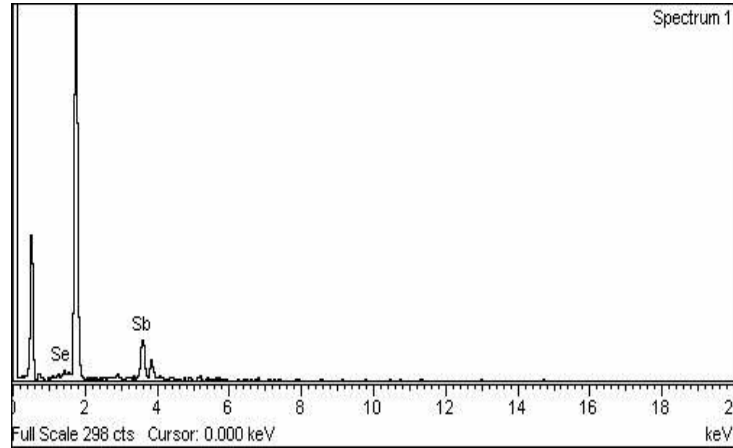


Figure 4.11: EDAX spectrum of SbSe3 as deposited thin film

4.2.6 Microstructural studies

Scanning electron microscopy (SEM) is done to observe the growth mechanism. The SEM micrographs of the sections of the films are shown in **figure 4.12**, where the results from as deposited and annealed types are compared. The left side micrograph represents as deposited SbSe1 thin film while the right micrograph represent the annealed thin film of the same. This micrograph reveals that as deposited film is not uniform in thickness. The presence of randomly spread thinner and thicker areas conform the growth of film by a three-dimensional growth mechanism in thin film preparation technique.

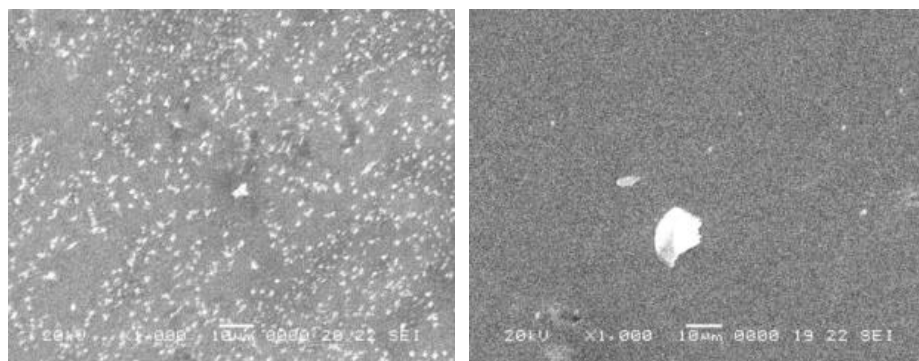


Figure 4.12: SEM micrograph of as deposited and annealed SbSe1 thin films respectively

When the film is annealed at vacuum with pressure $> 10^{-5}$ Torr for 2 hours at 473 K temperature, thickness distribution of the film becomes uniform as observed, over the film.

4.2.7 AFM studies

The surface morphological characteristics of these films are obtained from AFM studies. **Figure 4.13, 4.14** and **4.15** shows AFM image of as deposited and irradiated respective thin film surfaces grown on quartz substrates.

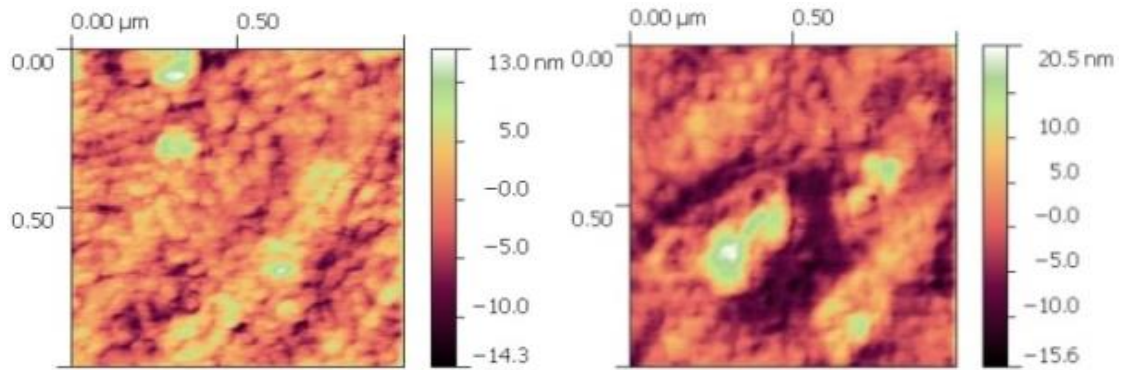


Figure 4.13: AFM 2-D images of as deposited and irradiated (fluence 5×10^{12} ions per cm^2) SbSe_3 bi-layer thin films

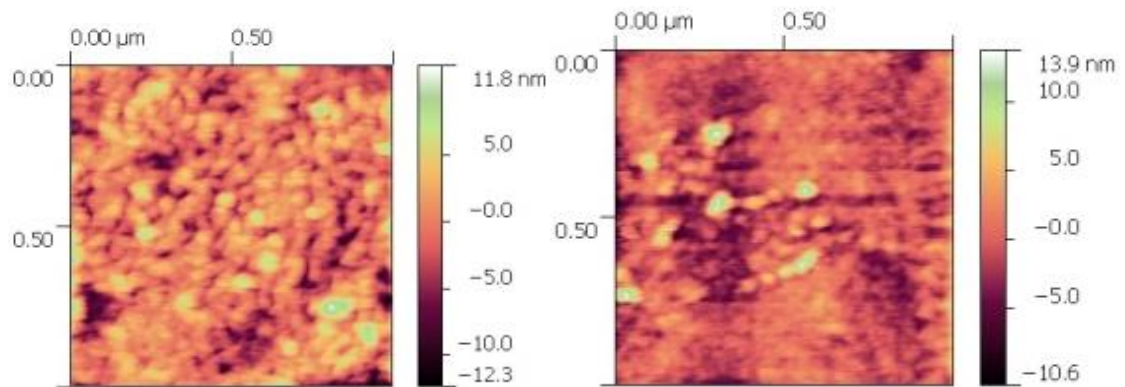


Figure 4.14: AFM 2-D images of as deposited and irradiated (fluence 5×10^{12} ions per cm^2) SbSe_2 bi-layer thin films

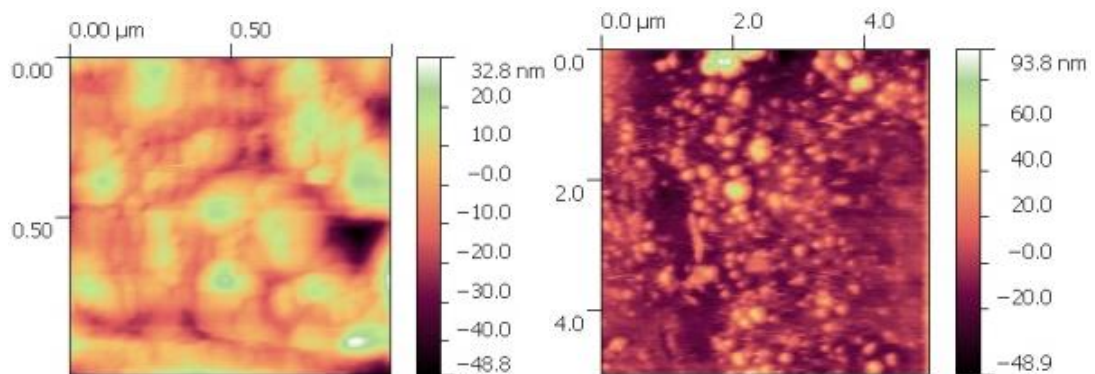


Figure 4.15: AFM 2-D images of as deposited and irradiated (fluence 5×10^{12} ions per cm^2) SbSe_1 bi-layer thin films

Sample	Particle size (nm) measured from AFM		rms roughness (nm) measured from AFM	
	As deposited	irradiated	As deposited	Irradiated
SbSe3	57.4	44.7	0.61	0.44
SbSe2	48.4	43.7	1.23	0.76
SbSe1	47.2	19.8	2.02	1.08

Table 4.5: Surface parameters calculated from AFM analysis for as deposited and irradiated samples respectively.

The particle size and root mean square (rms) roughness observed from AFM studies are listed in **table 4.5**.

The AFM studies indicate that with the increase in thickness of the Se layer from SbSe3 to SbSe1 the particle size decreases and rms roughness increases for both as deposited and irradiated thin films. From **table 4.5** it is also observed that due to irradiation with Ag^{+15} ions at fluence 5×10^{12} ions per cm^2 thin films particle size and rms roughness decreases.

The values from XRD and AFM (**table 4.5**) shows that crystallite size after irradiation increases while the particle size decreases. From the AFM images it seems, the observed particles are not single crystals but are made-up of few crystallites. It is observed that due to irradiation the particle size decreases than as deposited, but the crystallinity of the film improves much more than that of as deposited film.

References

- [1]. Magnetic Materials, Fundamentals and applications, 2nd ed. By Nicola A Spaldin
- [2]. David D Awschalom, Michael E Flatte *Nat. Phys.* **3** 153-159 (2007).
- [3]. M. N. Baibich, J. M. Broto, A. Fert, F. Nguyen Van Dau, F. Petroff *Phys. Rev. Lett.* **61** 2472-2475 (1988).
- [4]. K. W. Edmonds, K. Y. Wang, R. P. Campion, A. C. Neumann, R. S. Ferley, B. L. Gallagher, C. T. Foxon *Appl. Phys. Lett.* **81** 4991-4994 (2002).
- [5]. Scott A. Chambers and Robin. F. C. Farrow *MRS Bulletin* **28** 729-733 (2003).
- [6]. D. Chiba, K. Takamura, F. Matsukura and H. Ohno *Appl. Phys. Lett.* **82** 3020-3023 (2003).
- [7]. T. Dietl, H. Ohno, F. Matsukura, J. Cibert, and D. Ferrand *Science* **287** 1019-1022 (2000).
- [8]. T. Dietl, H. Ohno, and F. Matsukura *Phys. Rev. B* **63** 195205-195226 (2001).
- [9]. S. A. Gad, M. Boshta, A. M. Abo El-Soud, Y. A. el- Gendy *International journal of the Physical Sciences* **5** 1004-1008 (2010).
- [10]. S. M. Pawar, A.V. Moholkar, K. Y. Rajpure, C. H. Bhosale *Applied Surface Science* **253** 7313 (2007).
- [11]. S. Thanikaikarasan, K. Sundaram, T. Mahalingam, S. Velumani, Jin-Koo Rhee *Materials Science and Engineering B* **174** 242 (2010).
- [12]. J. A. Peters, N. D. Parashar, N. Rangaraju, BW Wessels *Phys. Rev. B* **82** 205207-205214 (2010).
- [13]. K. Ando, H. Saito, Jin Zhengwu, T. Fukumara, M. Kawasaki, Y. Matsumoto, H. Koinuma *J. Appl. Phys.* **89** 7284-7286 (2001).
- [14]. S. Riaz, S. Naseem, Y. B. Xu *J. Sol-Gel Technol.* **59** 584-590 (2011).

- [15]. H. A. Zayed, A. M. Abo-Elhoud, A. M. Ibrahim and M. A. Kenawy *J. Phys D: App. Phys.* **28** 770-773 (1995).
- [16]. M. J. Kang, S. Y. Choi, D. Wamwangi, K. Wang, C. Steimer, M. Wuttig *J. App. Phys.* **98** 014904-014909 (2005).
- [17]. DRS Somayajulu, Mukesh Chawda, Narendra Patel, Mitesh Sarkar, K.C. Sebastian, K. Venugopalan, A. Gupta *Appl. Phys. Lett.* **87** 242508-242510 (2005).
- [18]. Naveen Agrawal, Mitesh Sarkar, Mukesh Chawda and V Ganesan *Materials chemistry and physics* **143** 330-335 (2013).
- [19]. Y. Sun, S. Johnsen, P. Eklund, M. Sillassen, J. Bottiger, N. Oeschler, P. Sun, F. Steglich and B. B. Iversen *J. Appl. Phys.* **106** 033710-033713 (2009).
- [20]. Ye Sun, Stela Canulescu, Peijie Sun, Frank Steglich, Nini Pryds, Jorgen Schou, Bo Brummerstedt Iversen *Appl. Phys. A* **104** 883–887 (2011).
- [21]. Y. Sun, E. Zhang, S. Johnsen, M. Sillassen, P. Sun, F. Steglich, J. Bottiger, B. B. Iversen *Thin Solid films* **519** 5397-5402 (2011).
- [22]. C. L. Chien, Gang Xiao and K. M. Unruh *Phys. Rev. B* **32** 5582-5590 (1985).
- [23]. N. Badera, B. Godbole, S. B. Shrivastava, P. N. Vishwakarma, L. S. Sharath Chandra, Deepti Jain, V. G. Sathe, V. Ganesan *Sol. Energy Mater. Sol. Cells* **92** 1646-1651 (2008).
- [24]. F Abd El-Salam, M A Afifi, E Abd El-Wahabb *Vacuum* **44** 111 (1993).
- [25]. V. Damodar Das and P Gopal Ganesan *Semicond. Sci. Technol.* **12** 195–202 (1997).
- [26]. Vinay Ambegaokar, B. I. Halperin, J. S. Langer *Phys. Rev. B* **4** 2612-2620 (1971).
- [27]. Shubra Singh, M. S. Ramchandra Rao *Phys. Rev. B* **80** 045210-045219 (2009).
- [28]. A. D. Acharya, Shweta Moghe, Richa Panda, S.B. Shrivastava, Mohan

- Gangrade, T. Shripathi, D. M. Phase, V. Ganesan *Thin solid films* **525** 49-55 (2012).
- [29]. R Hussin, K L Choy and X Hou *J Nanosci Nanotechnol.* **11(9)** 8143 (2011)
- [30]. Yu K M Moll, A J Chan N Walnkiewicz and Beela P *Appl. Phys. Lett* **66** 2406 (1995).
- [31]. R. K. Mangal, B. Tripathi, M. Singh and Y K Vijay *Bull. Mater. Sci.* **30** 5 (2007).
- [32]. R. K. Mangal and Y K Vijay *Bull. Mater. Sci.* **30** 117 (2007).
- [33]. M. Singh and Y K Vijay *Appl. Surf. Sci.* **239** 79 (2004).
- [34]. P M P Salome, J Malaquias, P A Fernandes and A F da Cunha *J. Phys. D: Appl. Phys.* **43** 344501 (2010).
- [35]. Minghuang Huang, Carl Boone, Michelle Roberts, Don E. Savage, Max G. Lagally, Nakul Shaji, Hua Qin, Robert Blick, John A. Nairn and Feng Liu *Adv. Mater.* **17** 23 2860 (2005).
- [36]. James Hsu, Canek Fuentes- Hernandez, Alfred R. Ernst, Joel M. Hales, Joseph W. Perry and Bernard Kippelen *Optics Express* **20** 8 (2012).
- [37]. Tetsuya Nishida, Hisataka Sugiyama and Shinkichi Horigome *Jpn. J. Appl. Phys.* **34** 1562 (1995).
- [38]. Kai Liu, Zhong Yi Lu and Tao Xiang *Phy. Rev. B* **85** 235123 (2012).
- [39]. P P Pradyumanan and Swathikrishnan *Indian Journal of Pure and Applied Physics* **48** 115 (2010).
- [40]. K. Y. Rajpure, C. D. Lokhande, C. H. Bhosale *Thin Solid films* **311** 114 (1997).
- [41]. K Kolev, M. wautelet and L. D. Laude *Appl. Surf. Sci.* **46** 418 (1990).
- [42]. K. Kolev and L. D. Laude *Appl. Surf. Sci.* **54** 358 (1992).
- [43]. Yoon Shon, Young Hae Kwon, Sh. U. Yuldashev, Y. S. Park, D. J. Fu, D. Y. Kim, H. S. Kim and T. W. Kang *J. Appl. Phys.* **93** 1546 (2003).

- [44]. G. K. Williamson and W. H. Hall *Acta Metall.* **1** 22 (1953).
- [45]. V Damodar Das and P Gopal Ganesan *Semicond. Sci. Technol.* **12** 195 (1997).